Unit Cell Analysis of Cylindrical Conformal Connected Arrays

Roderick G. Tapia Barroso, *Graduate Student Member, IEEE*, and Daniele Cavallo, *Senior Member, IEEE*

***Abstract*—We present an analysis of cylindrical connected array unit cells. Analytical expressions of the active input impedance are derived for both connected slots and dipoles in the presence of a backing reflector. The dipoles and slots can be oriented along the circumferential or longitudinal directions in cylindrical coordinates. A study on the variation of impedance as a function of the radius of curvature is presented. Difficulties with the numerical implementation of high-order cylindrical Floquet modes are discussed. To solve these issues, a method is proposed to approximate the higher order mode component of the cylindrical array impedance with the one of the equivalent planar geometry. This approach is justified by the observation that the reactive energy associated with the unit cell is weakly dependent on the curvature.**

***Index Terms*—Active input impedance, connected arrays, cylindrical arrays, spectral domain method, wideband arrays.**

I. Introduction

WIDEBAND arrays capable of covering a large scan range have received increasing attention in the last decades. The broadband performance is specially advantageous in size-constrained platforms, where there is a growing need to integrate multiple functionalities in a single radiating aperture. Such platforms, for example, aircraft, uncrewed aerial vehicles, and other mobile platforms, may also benefit from conformal arrays to improve aerodynamic efficiency and for seamless integration [1], [2], [3], [4]. Furthermore, cylindrical arrays have also received attention for applications requiring 360° azimuthal scanning due to their scan-invariant directivity, sidelobe level, and polarization purity. These advantages have found applications for naval multifunction systems [5], for direction of arrival estimation in surveillance and navigation radars [6], and for polarimetric weather radars [7].

Common antenna solutions for ultrawideband arrays include the Vivaldi-type or flared notch arrays [8], [9], the tightly coupled dipoles [10], [11], and the connected slot array [12], [13]. These elements have also been recently used in cylindrical conformal configurations for Vivaldi arrays [5], tightly coupled arrays [14], [15], [16], and connected arrays [17], [18]. The last type is investigated in this article, with focus on the development of an efficient analysis method to estimate the active input impedance.

Received 30 July 2025; revised 15 December 2025; accepted 3 January 2026. Date of publication 21 January 2026; date of current version 9 April 2026. *(Corresponding author: Roderick G. Tapia Barroso.)*

The authors are with the Department of Microelectronics, Faculty of Electrical Engineering, Mathematics and Computer Science (EEMCS), Delft University of Technology, 2628 CD Delft, The Netherlands (e-mail: r.g.tapiabarroso@tudelft.nl; d.cavallo@tudelft.nl).

Digital Object Identifier 10.1109/TAP.2026.3654197

Regarding the analysis of cylindrical arrays, different methods have been presented in literature. Arrays of waveguide-fed slits on a conducting cylinder were studied in [19], based on a modal representation of the unit cell, to derive an analytical solution for the element pattern. A similar geometry was investigated in [20] to study the mutual coupling, using an eigenvalue analysis of the scattering matrix. A modal approach was also employed in [21] to study the mutual coupling in cylindrical slot arrays and in [22] to analyze cylindrical arrays of waveguides combined with frequency selective surfaces.

While analytical solutions exist only for simple array geometries, more general elements have been studied with method of moments analyses, either in the spectral [23] or in the spatial domain [24], [25]. To apply the spatial domain method of moments to cylindrical structures, particular effort has been made in the evaluation of the closed-form spatial Green's function of cylindrical stratified media, also addressing the singularity of the space-domain Green's function for observation points close to the source [26], [27], [28], [29].

In order to model with a method of moments the unit cell of a periodic cylindrical array, the periodic spectral domain Green's function can be used, as in [30] and [31]. This can be constructed starting from the spectral Green's function of cylindrically stratified media, which can be derived with the general procedure presented in [32] and [33], with the algorithm in [34], or with the network methods derived in [35] and [36].

The goal of this article is to analyze cylindrical connected arrays of dipoles and slots in the presence of backing reflectors or cavities, as shown in Fig. 1. The analysis includes both dipoles or slots oriented parallel to the cylinder axis or along the circumference, needed for dual-polarized cylindrical arrays applications. Similar geometries were previously studied in [37], but the solution was numerical, based on a method of moments approach. A summary of the methods to analyze cylindrical arrays is reported in Table I. Unlike previous works, in this article, we introduce analytical expressions of the active input impedance or admittance of cylindrical connected arrays, based on a spectral-domain method. Being the expressions analytical, they can be evaluated with extremely reduced computational resources, much faster than numerical methods, such as the method of moment or the finite element method. This speed-up can be especially beneficial for optimization of the geometrical parameters in cylindrical connected array designs.

The analysis of planar connected arrays was derived earlier in [38] and [39], leading to expressions of the input impedance

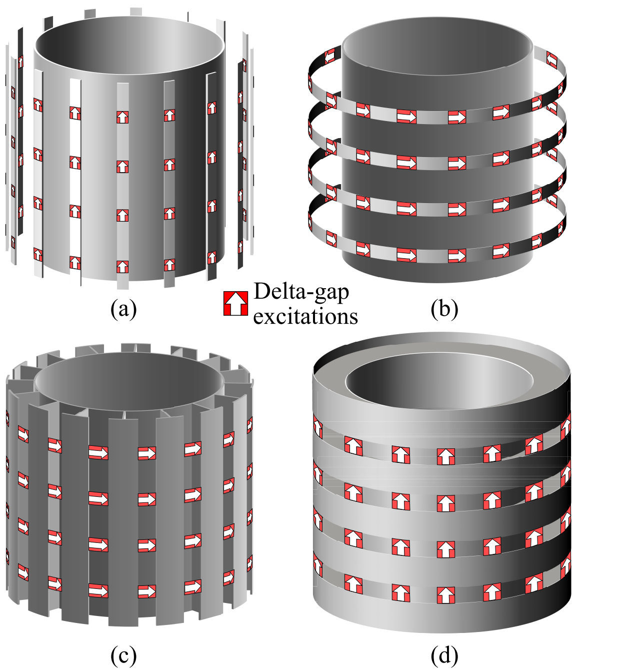

Fig. 1. Cylindrically connected arrays (a) z-connected dipoles, curved along their H-plane, (b) ϕ-connected dipoles, curved along their E-plane, (c) z-connected slots, curved along their E-plane, and (d) ϕ-connected slots, curved along their H-plane.

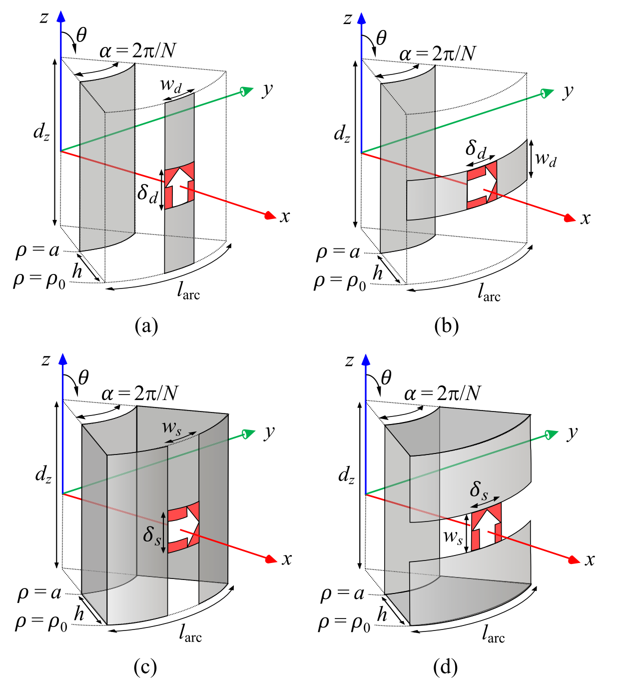

Fig. 2. Unit cells of (a) z-connected dipole array, (b) ϕ-connected dipole array, (c) z-connected slot array, and (d) ϕ-connected slot array.

TABLE I
COMPARISON WITH PREVIOUS WORKS ON ANALYSIS OF CYLINDRICAL GEOMETRIES

Ref.	Method	Type
[19], [20], [21], [22]	Mode matching	Numerical
[23]	Spectral-Domain MoM	Numerical
[24], [25], [28]	Space-Domain MoM	Numerical
[30], [31], [37]	Periodic MoM	Numerical
This work	Spectral-Domain Method	Semi-Analytical

in the form of double Floquet sums. To obtain similar formulas for cylindrical geometries, the explicit expression of the spectral dyadic Green's functions for both electric and magnetic sources is derived here.

The evaluation of the higher order Floquet modes requires the computation of Bessel and Hankel functions with large order and large argument, which can give rise to numerical overflow or underflow. We propose here a procedure to overcome these problems. The input impedance sum is split in a radiative component associated with the fundamental Floquet mode and a reactive component related to the higher order modes. It is shown that this latter component is weakly dependent on the radius of curvature and hence can be approximated by the reactive component of the equivalent planar geometry. This approach allows to completely avoid the numerical issues mentioned above.

Based on the expressions given here, we also study the variation of the input impedance of connected slots and dipoles as a function of the radius of curvature, to highlight the main difference between array elements curved in their E- or H-plane.

II. ACTIVE IMPEDANCE OF CYLINDRICAL CONNECTED DIPOLE ARRAYS

One of the advantages of planar connected arrays is that their active reflection coefficient can be calculated with analytical formulas in negligible computational time. That allows for efficient optimization of the unit cell performance as a function of the geometrical parameters [40]. Here, we derive expressions of the active impedance or admittance for cylindrical connected array unit cells, as depicted in Fig. 2.

A. Connected Dipoles Along z

The first case we consider is the case of connected dipoles oriented along z, as shown in Fig. 2(a). The array is periodic in the z-direction with period d_z and in the circumferential direction with period l_{arc}. As such, it is a 2-D periodic problems that can be analyzed through its unit cell. The circumferential periodicity can be related to the radius of curvature of the connected array ρ_0, as $\rho_0 = N l_{\text{arc}}/2\pi$, with N being the number of elements along ϕ. We can also define an unit cell angle $\alpha = 2\pi/N$, related to the curvature of the array. Furthermore, regarding the stratification, we consider a backing reflector in the form of a perfect electric conductor (PEC) cylinder with radius $\rho = a$ and thus located at a distance $h = \rho_0 - a$ from the radiating elements, which are assumed to be in free space. The delta-gap feed is characterized by length δ_d and the dipole's width is given by w_d. Following similar steps as the 2-D planar connected array [39], the active input admittance of the cylindrical connected dipole array can be calculated as

$$Y_{\text{d},z} = -\frac{1}{d_z} \sum_{m_z=-\infty}^{\infty} \frac{\operatorname{sinc}^2\left(\frac{k_{zm}\delta_d}{2}\right)}{D_{\text{d},z}(k_{zm})} \tag{1}$$

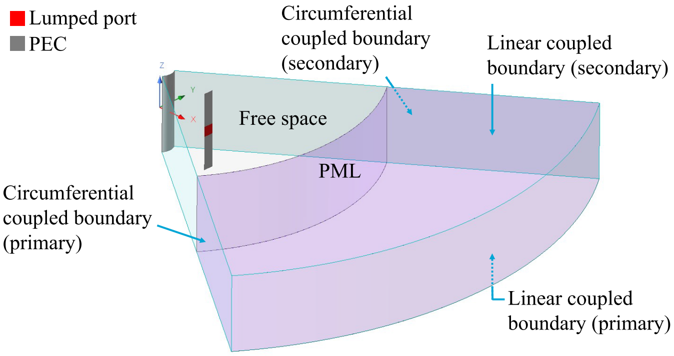

Fig. 3. Unit cell in HFSS for the modeling of cylindrical (connected) arrays.

where $\mathrm{sinc}(\xi) = \sin(\xi)/\xi$ and

$$D_{\mathrm{d},z}(k_{zm}) = \frac{2\pi}{\alpha} \sum_{m_\nu=-\infty}^{\infty} G^{EJ}_{\mathrm{cyl},zz}(\nu_m, k_{zm})\, J_0\left(\frac{\nu_m w_d}{2\rho_0}\right). \quad (2)$$

The function J_0 represents the Bessel function of the first kind and zeroth order. The input admittance is formulated as a double Floquet summation in m_z, associated with the periodicity of the feeds in z, and m_ν, associated with the circumferential periodicity along ϕ. The explicit formulas of the Floquet wavenumbers are given as follows:

$$k_{zm} = k_{z0} + \frac{2\pi m_z}{d_z}, \quad \nu_m = \nu_0 + \frac{2\pi m_\nu}{\alpha} \quad (3)$$

where $k_{z0} = k_0 \cos(\theta_0)$, k_0 is the free-space wavenumber, θ_0 is the scan angle with respect to the z-axis, and $\nu_0 \in [0, \pm 1, \pm 2, \ldots, \pm N-1]$ represents the phase-mode index associated with the ϕ-periodicity.

The expressions (1) and (2) resemble the case of the 2-D planar connected dipole array [39], but the key difference lies in the zz-component of the spectral dyadic Green's function $G^{EJ}_{\mathrm{cyl},zz}$, which represents the radiation of an electric point source located at $\rho = \rho_0$, radiating in the presence of a PEC cylinder of radius a. The procedure to derive the spectral dyadic Green's function in cylindrically stratified media is summarized given in the Appendix. The zz-component of the dyadic Green's function is calculated by using (36), (37), (53), and (54) from the Appendix, with the substitutions $m \to \nu_m$, $k_z \to k_{zm}$, $\rho = \rho' = \rho_0$, and $\hat{\alpha} = \hat{z}$, resulting in the following explicit expression:

$$G^{EJ}_{zz}(\nu_m, k_{zm}) = \frac{-k^2_{\rho m}}{4\omega\varepsilon_0} H^{(2)}_{\nu_m}(k_{\rho m}\rho_0) \times \left[J_{\nu_m}(k_{\rho m}\rho_0) - \frac{J_{\nu_m}(k_{\rho m}a)}{H^{(2)}_{\nu_m}(k_{\rho m}a)} H^{(2)}_{\nu_m}(k_{\rho m}\rho_0) \right]. \quad (4)$$

The functions J_{ν_m} and $H^{(2)}_{\nu_m}$ are the Bessel function of the first kind and the Hankel function of the second kind, respectively, both of order ν_m, ω is the angular frequency, ε_0 is the free-space permittivity, and $k_{\rho m} = (k_0^2 - k_{zm}^2)^{1/2}$.

The formulas are implemented in MATLAB and validated by comparison with the commercial software Ansys high-frequency structure simulator (HFSS) [41]. A typical HFSS unit cell model of a cylindrical array is shown in Fig. 3. The periodic boundary conditions in the circumferential direction are implemented as slanted planes, while the periodic boundaries in the direction with no curvature are parallel planes. A perfect matching layer (PML) is used to avoid reflections and simulate a radiation boundary condition. As an example, we consider an array with $N = 5$, $d_z = l_{\mathrm{arc}} = 0.4\lambda_0$, and $h = \lambda_0/4$, with λ_0 being the wavelength at the frequency f_0, and $w_d = \delta_d = \lambda_0/20$. The active input impedance $Z_{\mathrm{d},z}$ of the considered unit cells, that is, the reciprocal of the admittance defined in (1), is shown in Fig. 4(a), assuming equal phase excitation for all array elements. A good comparison with HFSS can be observed. A similar agreement is observed in Fig. 4(b), for scanning to $\theta = 60°$, corresponding to each element pointing to 30° from the radial direction ($\hat{x}$) in its xz plane, according to the reference system in Fig. 2(a).

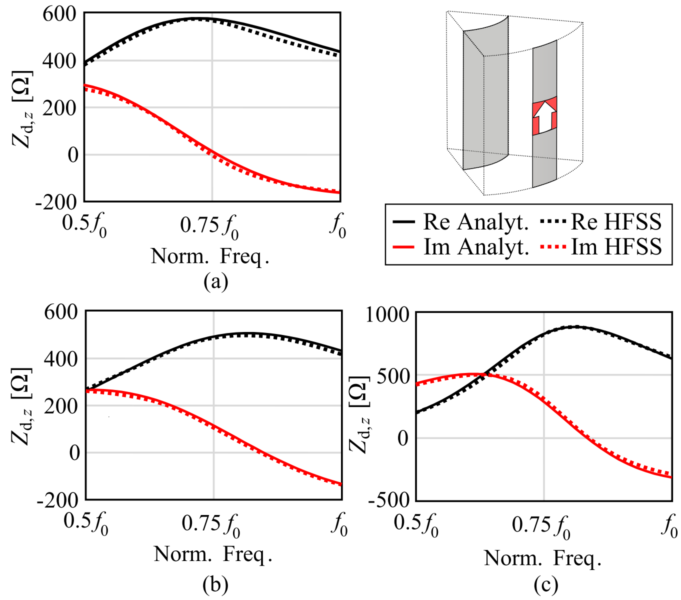

Fig. 4. Active input impedance of the z-connected dipole array for elements excited with (a) equal phase, (b) pointing to $\theta = 60°$, and (c) phase mode 1 (i.e., $\nu_0 = 1$). Comparison between analytical expressions and Ansys HFSS is shown, for $w_d = \delta_d = \lambda_0/20$, $d_z = l_{\mathrm{arc}} = 0.4\lambda_0$, and $h = \lambda_0/4$, with λ_0 being the wavelength at the frequency f_0 and $N = 5$.

As a last comparison, we consider the configuration with $\nu_0 = 1$. This corresponds to the unit cells having progressive phase shifts of $2\pi\nu_0/N = 72°$ along the circumferential direction. The correspondent input impedance is shown in Fig. 4(c) and agrees well with HFSS simulated results. The case of phase-mode index $\nu_0 = 1$ corresponds to a phase variation of 2π along the array circumference. This can be visualized in Fig. 5, where the electric near-field distribution of the array on the plane $z = 0$, simulated with HFSS, is shown for $\nu_0 = 0$ and $\nu_0 = 1$.

B. Connected Dipoles Along ϕ

For dipoles connected in the circumferential direction, as shown in Fig. 2(b), the active input admittance is given by

$$Y_{\mathrm{d},\phi} = -\frac{2}{\rho_0} \sum_{m_\nu=-\infty}^{\infty} \frac{\mathrm{sinc}^2\left(\frac{\nu_m \delta_d}{2\rho_0}\right)}{D_{\mathrm{d},\phi}(\nu_m)} \quad (5)$$

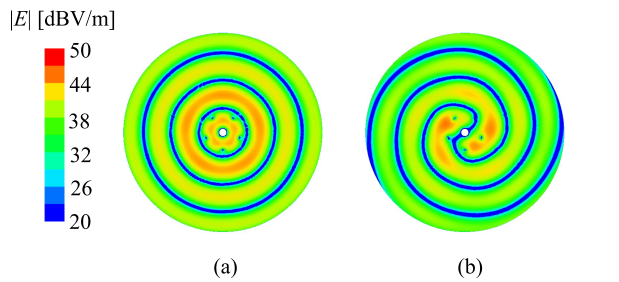

Fig. 5. Magnitude of the electric near field on the plane $z = 0$, for the array of dipoles oriented along z, simulated with HFSS (a) $\nu_0 = 0$ and (b) $\nu_0 = 1$.

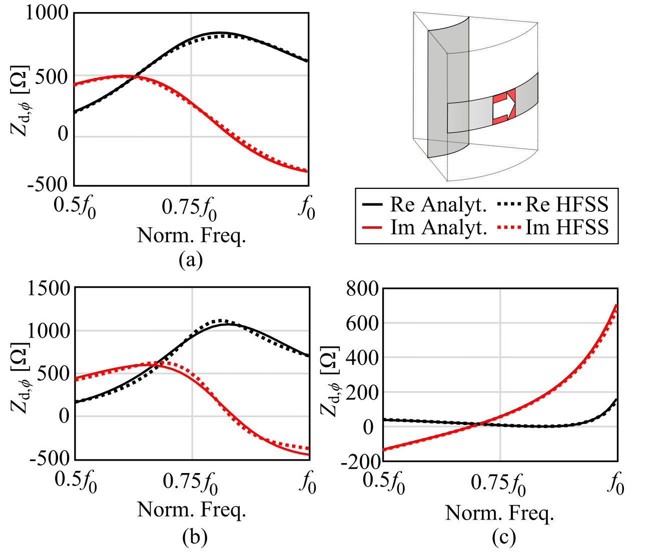

Fig. 6. Active input impedance of the ϕ-connected dipole array for elements excited with (a) equal phase, (b) pointing to $\theta = 60°$, and (c) for $\nu_0 = 1$. Comparison between analytical expressions and Ansys HFSS is shown, for the same geometrical parameters as shown in Fig. 4.

with

$$D_{d,\phi}(\nu_m) = \frac{1}{d_z}\sum_{m_z=-\infty}^{\infty} G^{EJ}_{\mathrm{cyl},\phi\phi}(\nu_m, k_{zm})\, J_0\left(\frac{k_{zm} w_d}{2}\right). \quad (6)$$

The $\phi\phi$-component of the spectral dyadic Green's function can be found by using the expressions reported given in the Appendix, more specifically by using (42), (53), and (54) with $\hat{\alpha} = \hat{\phi}$, resulting in

$$\begin{aligned} G^{EJ}_{\phi\phi}(\nu_m, k_{zm}) = -\frac{1}{4\omega\varepsilon_0}\Bigg\{ &\frac{\nu_m^2 k_{zm}^2}{k_{\rho m}^2 \rho_0^2} \\ &\times \left[J_{\nu_m}(k_{\rho m}\rho_0) - \frac{J_{\nu_m}(k_{\rho m}a)}{H^{(2)}_{\nu_m}(k_{\rho m}a)} H^{(2)}_{\nu_m}(k_{\rho m}\rho_0)\right] H^{(2)}_{\nu_m}(k_{\rho m}\rho_0) \\ &+ k_0^2 \left[J'_{\nu_m}(k_{\rho m}\rho_0) - \frac{J'_{\nu_m}(k_{\rho m}a)}{H^{(2)\prime}_{\nu_m}(k_{\rho m}a)} H^{(2)\prime}_{\nu_m}(k_{\rho m}\rho_0)\right] H^{(2)\prime}_{\nu_m}(k_{\rho m}\rho_0) \Bigg\} \end{aligned} \quad (7)$$

where the primed functions denote the derivative of these functions with respect to their argument.

The active impedance calculated with the given formulas is compared with HFSS simulations in Fig. 6(a)–(c), for equal phase excitation, for scanning to $\theta = 60°$, and for $\nu_0 = 1$, respectively. One can note that, for the last scanning configuration, the ϕ-oriented dipoles have very low input resistance due to a resonances of the entire circular ring of dipoles.

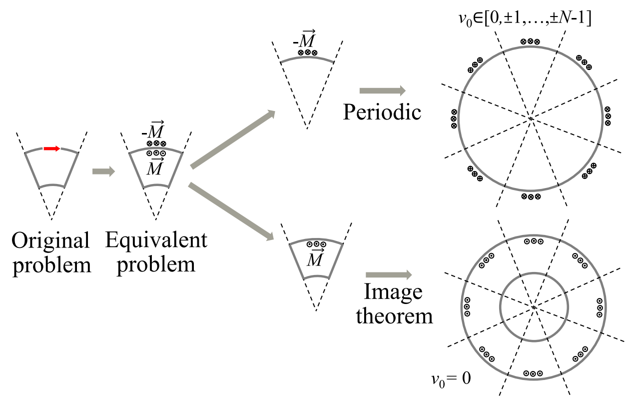

Fig. 7. Separation of the slot problem into external and internal problems; application of the periodic boundary conditions and the image theorem.

III. Active Impedance of Cylindrical Connected Slot Arrays

A. Connected Slots Along z

For a connected slot array along z, shown in Fig. 2(c), or equivalently an E-plane curved connected slot array, the formulation is similar and, due to duality, the input impedance is given as follows:

$$Z_{s,z} = -\frac{1}{d_z}\sum_{m_z=-\infty}^{\infty}\frac{\mathrm{sinc}^2\left(\frac{k_{zm}\delta_s}{2}\right)}{D_{s,z}(k_{zm})} \quad (8)$$

with

$$D_{s,z}(k_{zm}) = \frac{2\pi}{\alpha}\sum_{m_\nu=-\infty}^{\infty} G^{HM}_{\mathrm{cyl},zz}(\nu_m, k_{zm})\, J_0\left(\frac{\nu_m w_s}{2\rho_0}\right). \quad (9)$$

In the analysis of the connected slot unit cell, the original problem of a slot excited with a delta-gap source can be replaced with an equivalent problem, where the slot is filled with PEC and two equivalent surface magnetic currents (equal and opposite) are located above and below the metal, as described in Fig. 7. Thus, the total Green's function can be split in two components, one representing the external problem of a magnetic source on a PEC cylinder and one representing the internal problem of a magnetic current radiating in a coaxial cavity. This is mathematically represented as follows:

$$G^{HM}_{\mathrm{cyl},zz}(\nu_m, k_{zm}) = G^{HM}_{zz,\mathrm{ext}}(\nu_m, k_{zm}) + G^{HM}_{zz,\mathrm{cav}}(\nu_m, k_{zm}). \quad (10)$$

The Green's function for the external problem is derived from (36), (38), (53), and (54) given in the Appendix, with $\overline{\mathbf{R}}_{\mathrm{ext}}(\rho_0)$ and with the substitutions $m \to \nu_m$, $k_z \to k_{zm}$, $\rho = \rho' = \rho_0$, and $\hat{\alpha} = \hat{z}$, which results in

$$\begin{aligned} G^{HM}_{zz,\mathrm{ext}}(\nu_m, k_{zm}) = &\frac{-k_{\rho m}^2}{4\omega\mu_0} H^{(2)}_{\nu_m}(k_{\rho m}\rho_0) \\ &\times \left[J_{\nu_m}(k_{\rho m}\rho_0) - \frac{J'_{\nu_m}(k_{\rho m}\rho_0)}{H^{(2)\prime}_{\nu_m}(k_{\rho m}\rho_0)} H^{(2)}_{\nu_m}(k_{\rho m}\rho_0)\right] \end{aligned} \quad (11)$$

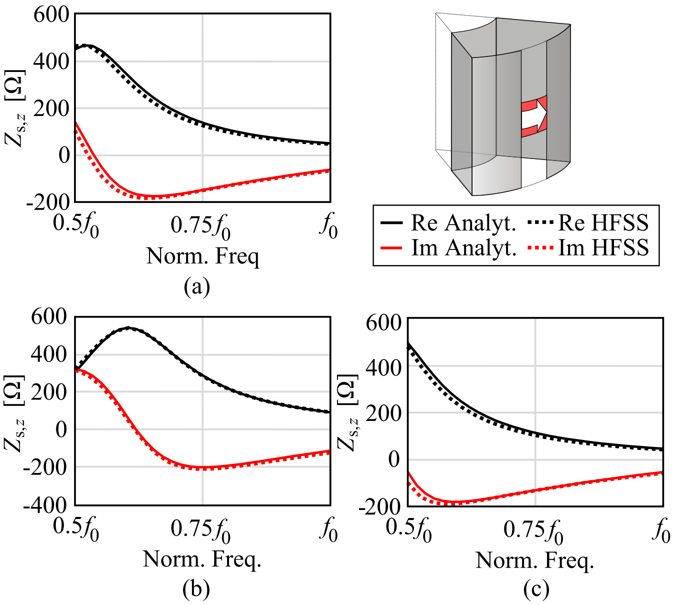

Fig. 8. Active input impedance of the z-connected slot array for elements excited with (a) equal phase, (b) pointing to $\theta_0 = 60°$, and (c) for $\nu_0 = 1$. Comparison between analytical expressions and Ansys HFSS is shown, for the same geometrical parameters as in Fig. 4, with $w_s = \delta_s = \lambda_0/20$.

where μ_0 is the free-space permeability.

For the coaxial cavity problem, by using (36) and (38) in (57), the Green's function can be derived explicitly as

$$G^{HM}_{zz,\mathrm{cav}}(\nu_m, k_{zm}) = \frac{-k_{\rho m}^2}{4\omega\mu_0}\left\{J_{\nu_m}(k_{\rho m}\rho_0)\, H^{(2)}_{\nu_m}(k_{\rho m}\rho_0) - H^{(2)}_{\nu_m}(k_{\rho m}\rho_0)\, R_1 - J_{\nu_m}(k_{\rho m}\rho_0)\, R_2\right\}. \quad (12)$$

It should be noted that the coefficients R_1 and R_2, due to the multiple reflections from the boundaries, depend on $\nu_m, k_{\rho m}$, and ρ_0, but this has been suppressed in (12) for the sake of compactness. The expressions of these coefficients are as follows:

$$R_1(\nu_m, k_{\rho m}, a, \rho_0) = J'_{\nu_m}(k_{\rho m}a) \times \frac{H^{(2)}_{\nu_m}(k_{\rho m}\rho_0)\, J'_{\nu_m}(k_{\rho m}\rho_0) - H^{(2)\prime}_{\nu_m}(k_{\rho m}\rho_0)\, J_{\nu_m}(k_{\rho m}\rho_0)}{J'_{\nu_m}(k_{\rho m}\rho_0)\, H^{(2)\prime}_{\nu_m}(k_{\rho m}a) - H^{(2)\prime}_{\nu_m}(k_{\rho m}\rho_0)\, J'_{\nu_m}(k_{\rho m}a)} \quad (13)$$

$$R_2(\nu_m, k_{\rho m}, a, \rho_0) = H^{(2)\prime}_{\nu_m}(k_{\rho m}\rho_0) \times \frac{J_{\nu_m}(k_{\rho m}\rho_0)\, H^{(2)\prime}_{\nu_m}(k_{\rho m}a) - H^{(2)}_{\nu_m}(k_{\rho m}\rho_0)\, J'_{\nu_m}(k_{\rho m}a)}{J'_{\nu_m}(k_{\rho m}\rho_0)\, H^{(2)\prime}_{\nu_m}(k_{\rho m}a) - H^{(2)\prime}_{\nu_m}(k_{\rho m}\rho_0)\, J'_{\nu_m}(k_{\rho m}a)}. \quad (14)$$

Cavity walls at $\phi = \pm\alpha/2$ are considered [Fig. 2(c)], to avoid modes propagating between the slot surface and the backing reflector. To account for these walls, ν_m in $G^{HM}_{zz,\mathrm{cav}}$ must be always evaluated for $\nu_0 = 0$. This is because, as shown in Fig. 7, in the internal problem, no phase difference exists when applying the image theorem to the side walls. On the contrary, in the external problem, the periodic boundary conditions allow for a possible phase progression along the circumference.

The analytical expression of the active impedance is compared with HFSS in Fig. 8(a)–(c), for different scanning configurations, showing good agreement.

B. Connected Slots Along ϕ

Finally, we consider the slot curved along its H-plane and thus connected along the ϕ-direction, as depicted in Fig. 2(d). The input impedance can be calculated as follows:

$$Z_{s,\phi} = -\frac{2}{\rho_0}\sum_{m_\nu=-\infty}^{\infty}\frac{\mathrm{sinc}^2\left(\frac{\nu_m\delta_s}{2\rho_0}\right)}{D_{s,\phi}(\nu_m)} \quad (15)$$

with

$$D_{s,\phi}(\nu_m) = \frac{1}{d_z}\sum_{m_z=-\infty}^{\infty} G^{HM}_{\mathrm{cyl},\phi\phi}(\nu_m, k_{zm})\, J_0\left(\frac{k_{zm}w_s}{2}\right). \quad (16)$$

Similar to the previous case, the Green's function is the sum of two terms

$$G^{HM}_{\mathrm{cyl},\phi\phi}(\nu_m, k_{zm}) = G^{HM}_{\phi\phi,\mathrm{ext}}(\nu_m, k_{zm}) + G^{HM}_{\phi\phi,\mathrm{cav}}(\nu_m, k_{zm}) \quad (17)$$

which can be derived by applying (42) with $\hat{\alpha} = \hat{\phi}$ resulting, for the external problem, in

$$G^{HM}_{\phi\phi,\mathrm{ext}}(\nu_m, k_{zm}) = \frac{-1}{4\omega\mu_0}\left\{\frac{\nu_m^2 k_{zm}^2}{k_{\rho m}^2\rho_0^2}\left[J_{\nu_m}(k_{\rho m}\rho_0) - \frac{J'_{\nu_m}(k_{\rho m}\rho_0)}{H^{(2)\prime}_{\nu_m}(k_{\rho m}\rho_0)} H^{(2)}_{\nu_m}(k_{\rho m}\rho_0)\right] \times H^{(2)}_{\nu_m}(k_{\rho m}\rho_0) - k_0^2\left[J'_{\nu_m}(k_{\rho m}\rho_0) - \frac{J_{\nu_m}(k_{\rho m}\rho_0)}{H^{(2)}_{\nu_m}(k_{\rho m}\rho_0)} H^{(2)\prime}_{\nu_m}(k_{\rho m}\rho_0)\right] H^{(2)\prime}_{\nu_m}(k_{\rho m}\rho_0)\right\} \quad (18)$$

and, for the internal coaxial cavity problem, in

$$G^{HM}_{\phi\phi,\mathrm{cav}}(\nu_m, k_{zm}) = \frac{1}{4\omega\mu_0}\left\{\frac{\nu_m^2 k_{zm}^2}{k_{\rho m}^2\rho_0^2}\left[J_{\nu_m}(k_{\rho m}\rho_0)\, H^{(2)}_{\nu_m}(k_{\rho m}\rho_0) - H^{(2)}_{\nu_m}(k_{\rho m}\rho_0)\, R_1 - J_{\nu_m}(k_{\rho m}\rho_0)\, R_2\right] + k_0^2\left[J'_{\nu_m}(k_{\rho m}\rho_0)\, H^{(2)\prime}_{\nu_m}(k_{\rho m}\rho_0) - H^{(2)\prime}_{\nu_m}(k_{\rho m}\rho_0)\, R_3 - J'_{\nu_m}(k_{\rho m}\rho_0)\, R_4\right]\right\} \quad (19)$$

with the coefficients R_3 and R_4 given as follows:

$$R_3(\nu_m, k_{\rho m}, a, \rho_0) = J_{\nu_m}(k_{\rho m}a) \times \frac{H^{(2)\prime}_{\nu_m}(k_{\rho m}\rho_0)\, J_{\nu_m}(k_{\rho m}\rho_0) - H^{(2)}_{\nu_m}(k_{\rho m}\rho_0)\, J'_{\nu_m}(k_{\rho m}\rho_0)}{J_{\nu_m}(k_{\rho m}\rho_0)\, H^{(2)}_{\nu_m}(k_{\rho m}a) - H^{(2)}_{\nu_m}(k_{\rho m}\rho_0)\, J_{\nu_m}(k_{\rho m}a)} \quad (20)$$

$$R_4(\nu_m, k_{\rho m}, a, \rho_0) = H^{(2)}_{\nu_m}(k_{\rho m}\rho_0) \times \frac{J'_{\nu_m}(k_{\rho m}\rho_0)\, H^{(2)}_{\nu_m}(k_{\rho m}a) - H^{(2)\prime}_{\nu_m}(k_{\rho m}\rho_0)\, J_{\nu_m}(k_{\rho m}a)}{J_{\nu_m}(k_{\rho m}\rho_0)\, H^{(2)}_{\nu_m}(k_{\rho m}a) - H^{(2)}_{\nu_m}(k_{\rho m}\rho_0)\, J_{\nu_m}(k_{\rho m}a)}. \quad (21)$$

Because of the cavity walls assumed to be at $z = \pm d_z/2$ [Fig. 2(d)], k_{zm} in $G^{HM}_{\phi\phi,\mathrm{cav}}$ must have $k_{z0} = 0$.

The analytical expression of the active impedance is in good agreement with HFSS in Fig. 9(a)–(c), for different scanning configurations.

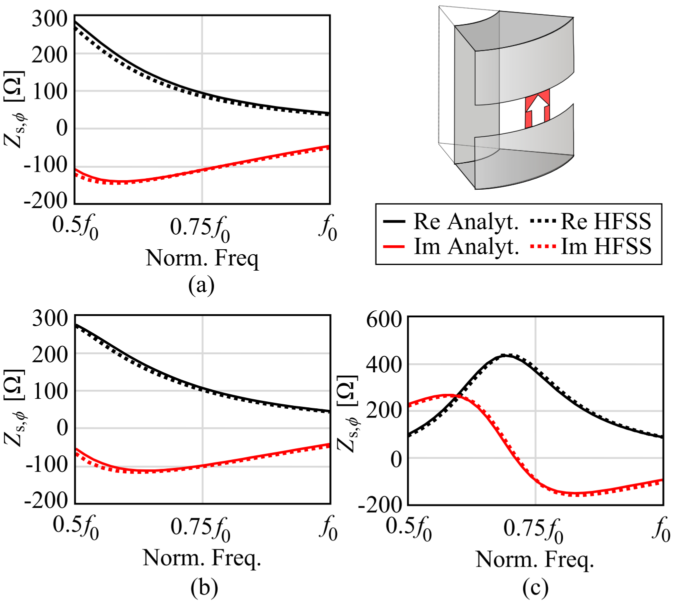

Fig. 9. Active input impedance of the ϕ-connected slot array for elements excited with (a) equal phase, (b) pointing to $\theta_0 = 60°$, and (c) $\nu_0 = 1$. Comparison between analytical expressions and Ansys HFSS is shown, for the same geometrical parameters as in Fig. 4, with $w_s = \delta_s = \lambda_0/20$.

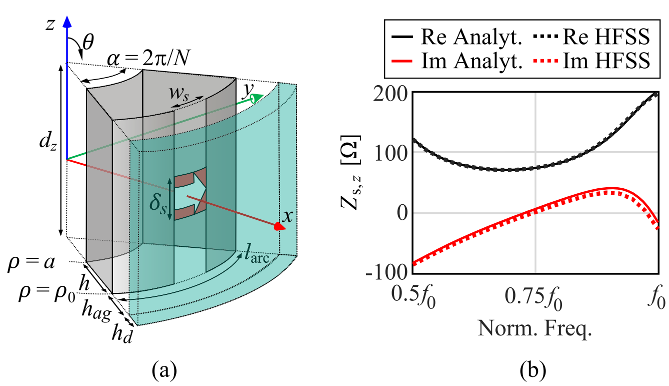

Fig. 10. (a) Unit cell of the z-connected slot array loaded by a dielectric slab and (b) active input impedance comparison between analytical expressions and Ansys HFSS, for $w_s = \lambda_0/25, \delta_s = \lambda_0/10$, $d_z = l_{\text{arc}} = 0.4\lambda_0$, $h = \lambda_0/4$, $h_{ag} = \lambda_0/13$, and $h_d = \lambda_0/20$, with λ_0 being the wavelength at the frequency f_0, and $N = 5$.

C. Dielectric Loading

Sections II, III-A, and III-B showed the explicit Green's function for the evaluation of connected arrays in free space. In this section, we show a generalization for a z-connected slot array loaded by a thin dielectric slab, as shown in Fig. 10(a). In this example, we consider a dielectric slab with relative permittivity $\varepsilon_r = 9$ and thickness $h_d = \lambda_0/20$, at distance $h_{ag} = \lambda_0/13$ from the slots. The input impedance can be calculated using the formulas (8)–(10). However, due to the presence of the dielectric, $G^{HM}_{zz,\text{ext}}(\nu_m, k_{zm})$ must be calculated taking into account the generalized reflection matrices as described given in the Appendix. The active input impedance calculated with the method presented here is shown in Fig. 10(b) and agrees well with the HFSS results. In terms of computation time, our method can evaluate the impedance in Fig. 10(b) in 0.13 s, while HFSS takes 119 s.

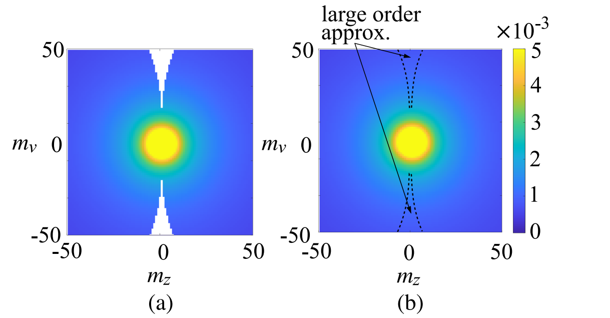

Fig. 11. $|G|$ versus mode indexes m_ν and m_z, for $N = 8$. (a) Default implementation of Bessel and Hankel functions and (b) asymptotic approximation for large order of Bessel and Hankel functions.

IV. Analysis of Impedance Versus Radius of Curvature

A. Asymptotic Evaluation of Bessel/Hankel Functions

The validations shown in Sections II and III assumed a small radius of curvature with $N = 5$. When implementing the same formulas for larger N, some numerical problems occur in the evaluation of Hankel and Bessel functions of large order and/or large argument. To highlight this issue, Fig. 11(a) reports the magnitude of the function

$$G = H^{(2)}_{\nu_m}\left(k_{\rho m}\rho_0\right)\left[J_{\nu_m}\left(k_{\rho m}\rho_0\right) - \frac{J_{\nu_m}(k_{\rho m}a)}{H^{(2)}_{\nu_m}(k_{\rho m}a)}H^{(2)}_{\nu_m}\left(k_{\rho m}\rho_0\right)\right] \quad (22)$$

used both in (4) and (7), versus the mode indexes m_z and m_ν, for $N = 8$. The white areas indicate undefined numerical values ("not a number" in MATLAB) resulting from overflow or underflow of the MATLAB built-in Bessel and Hankel functions. To overcome this problem, large order approximations can be implemented [43]

$$J_m(x) \sim \frac{1}{\sqrt{2\pi m}}\left(\frac{ex}{2m}\right)^m \quad (23)$$

$$H^{(2)}_m(x) \sim j\frac{2}{\sqrt{\pi m}}\left(\frac{ex}{2m}\right)^{-m} \quad (24)$$

with e being the Euler constant. Other known approximations of the Bessel and Hankel functions can be found in [23] and [44]. Expressions (23) and (24) can be used in (22) to approximate it as follows:

$$G \sim \frac{j}{\pi\nu_m}\left[1 - \left(\frac{a}{\rho_0}\right)^{2\nu_m}\right]. \quad (25)$$

By using this approximation, the undefined numerical values in Fig. 11(a) can be computed resulting in Fig. 11(b). Please note that the approximations in (23) and (24) are only valid for large order m with respect to the argument $m \gg x$.

When we consider a larger radius of curvature, for example, $N = 80$, the numerical instabilities extend to a larger part of the computation domain [Fig. 12(a)]. One can note that, for $N = 80$, the range [−50, 50] for the modes m_ν and m_z corresponds Bessel/Hankel functions with orders in the range [−4000, 4000] and arguments up to $\approx -4000j$.

The numerical overflows and underflows are not only associated with the large order but also with the large argument

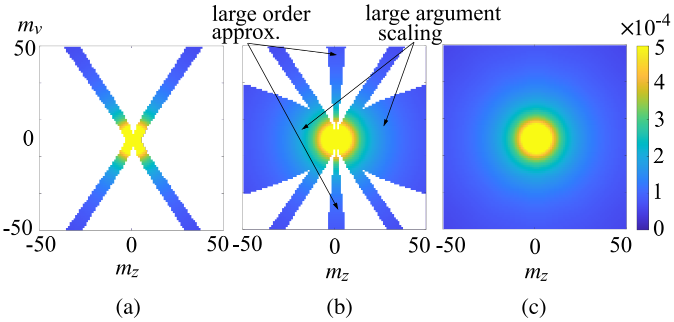

Fig. 12. $|G|$ versus mode indexes m_ν and m_z, for $N = 80$. (a) Default implementation of Bessel and Hankel functions, (b) large-order approximation and scaling of Bessel and Hankel functions for large argument, and (c) bilinear interpolation to recover the missing values.

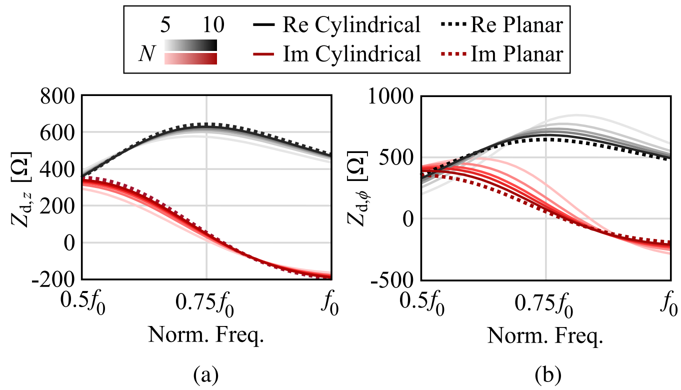

Fig. 13. Active input impedance of connected dipole unit cell versus N (a) dipoles along z and (b) dipoles along ϕ. The geometrical parameters are as defined in Fig. 4, for varying N and the elements are excited with equal phase.

evaluation of the Bessel and Hankel functions. The approximation in (25) can be used to recover the values in a small region around the axis $m_z = 0$, as shown in Fig. 12(b). For the numerical instability associated with the large argument, one can use MATLAB's built-in scaling option for the computation of Bessel and Hankel functions [45]. This consists in defining a modified version of the functions as follows:

$$\tilde{J}_m(x) = e^{-|\Im\{x\}|} J_m(x) \tag{26}$$

$$\tilde{H}_m^{(2)}(x) = e^{jx} H_m^{(2)}(x) \tag{27}$$

where $\Im\{x\}$ represents the imaginary part of the argument. Expression (22) can be then calculated with the scaled functions, with an a posteriori correction to account for the scaling as follows:

$$\begin{aligned} G = {} & \tilde{J}_{\nu_m}\left(k_{\rho m}\rho_0\right) \tilde{H}_{\nu_m}^{(2)}\left(k_{\rho m}\rho_0\right) \\ & - \frac{\tilde{J}_{\nu_m}(k_{\rho m}a)}{\tilde{H}_{\nu_m}^{(2)}(k_{\rho m}a)} \tilde{H}_{\nu_m}^{(2)}\left(k_{\rho m}\rho_0\right) \tilde{H}_{\nu_m}^{(2)}\left(k_{\rho m}\rho_0\right) e^{-2jk_{\rho m}(\rho_0 - a)}. \end{aligned} \tag{28}$$

Using (28), the area around the $m_\nu = 0$ axis can be computed as shown in Fig. 12(b). However, the solution is not complete, as there are still numerically undefined regions. In order to recover the whole matrix, we use a bilinear interpolation to approximate the invalid numbers, resulting in Fig. 12(c).

For the case of the ϕ-oriented dipoles, we can apply the same scaling for the large argument, while for the large-order approximation, using (23) and (24) in (7), together with the recurrence relations to evaluate the derivatives J'_{ν_m} and $H_{\nu_m}^{(2)\prime}$, gives the following large order approximation:

$$\begin{aligned} G_{\phi\phi}^{EJ}(\nu_m, k_{zm}) \sim {} & \frac{-j}{4\omega\pi\varepsilon_0 k_{\rho m}^2 \rho_0^2} \\ & \times \left\{ \nu_m k_{\rho m}^2 \left[1 - \left(\frac{a}{\rho_0}\right)^{2\nu_m} \right] - k_0^2 \left(\frac{a}{\rho_0}\right)^{2\nu_m} \right\}. \end{aligned} \tag{29}$$

The proposed method allows the study of the active impedance of the cylindrical connected dipoles as a function of the radius of curvature. In Fig. 13, the impedance of cylindrical dipole arrays curved in their E- or H-plane is shown for N varying from five to ten. For comparison, the solution of an equivalent planar structure ($N \to \infty$) is also reported, to verify that the impedance of array with increasing radius of curvature converges to the planar array solution. From this result, one can also observe that the array curved in its E-plane is more affected by the curvature and converges slower to the planar case, compared to the array curved in its H-plane. This can be explained by the fact that a stronger mutual coupling occurs in the E-plane, compared to the H-plane, due to the electrical connection of the dipoles [42].

B. Decomposition of the Input Impedance

It should be mentioned that deriving (29) is algebraically intense and is impractical for the connected slots, because of the longer expressions of the Green's functions. For this reason, we introduce an alternative approach to solve the numerical issues, based on comparing the higher order component of the input impedance of the cylindrical array with the one of the equivalent planar structure.

As an example, we look at the dipoles connected along ϕ, as they show larger deviation with respect to the planar case. The input impedance, calculated as reciprocal of (5), is written as a modal expansion with mode indexes m_ν and m_z. By splitting the m_ν-sum in $m_\nu = 0$ and $m_\nu \neq 0$ and the m_z-sum in $m_z = 0$ and $m_z \neq 0$, we can separate the impedance in three terms as follows:

$$Z_{d,\phi} = Z_{d,\phi}^{cap} \parallel \left(Z_{d,\phi}^{ind} + Z_{d,\phi}^{00}\right) \tag{30}$$

where the capacitance associated with the gap is represented by the higher order modes in m_ν and is defined as

$$Y_{d,\phi}^{cap} = \frac{1}{Z_{d,\phi}^{cap}} = -\frac{2}{\rho_0} \sum_{m_\nu \neq 0} \frac{\operatorname{sinc}^2\left(\frac{\nu_m \delta_d}{2\rho_0}\right)}{D_{d,\phi}(\nu_m)}. \tag{31}$$

The dipole inductance, associated with the modes $m_z \neq 0$, is defined as

$$Z_{d,\phi}^{ind} = -\frac{\rho_0}{2d_z} \frac{\sum_{m_z \neq 0} G_{cyl,\phi\phi}^{EJ}(\nu_0, k_{zm}) J_0\left(\frac{k_{zm} w_d}{2}\right)}{\operatorname{sinc}^2\left(\frac{\nu_0 \delta_d}{2\rho_0}\right)} \tag{32}$$

while the term associated with the fundamental Floquet mode ($m_\nu = m_z = 0$) gives

$$Z_{d,\phi}^{00} = -\frac{\rho_0}{2d_z} \frac{G_{cyl,\phi\phi}^{EJ}(\nu_0, k_{z0}) J_0\left(\frac{k_{z0} w_d}{2}\right)}{\operatorname{sinc}^2\left(\frac{\nu_0 \delta_d}{2\rho_0}\right)}. \tag{33}$$

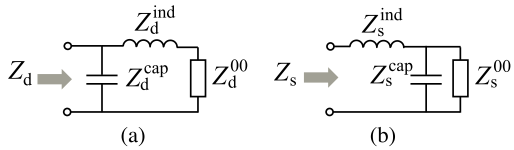

Fig. 14. Equivalent circuit representing the active input impedance of connected arrays of (a) dipoles and (b) slots.

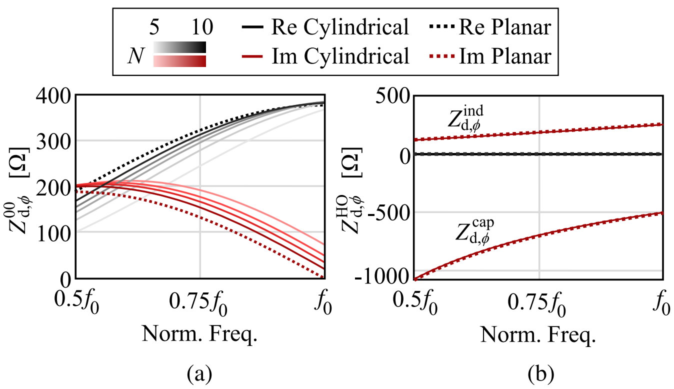

Fig. 15. Active input impedance of connected ϕ-oriented dipole unit cell versus N. (a) Fundamental Floquet mode and (b) higher order modes. The geometrical parameters are as defined in Fig. 4, for varying N and the elements are excited with equal phase.

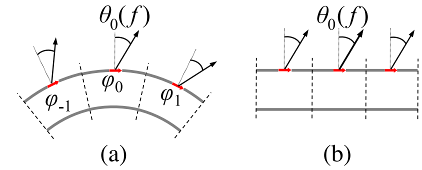

Fig. 16. (a) Cylindrical array of connected dipoles with phase shift $\phi_1 - \phi_0 = \phi_0 - \phi_{-1} = \Delta\phi = 2\pi\nu_0/N$ and (b) equivalent planar array to evaluate the reactive component of the input impedance.

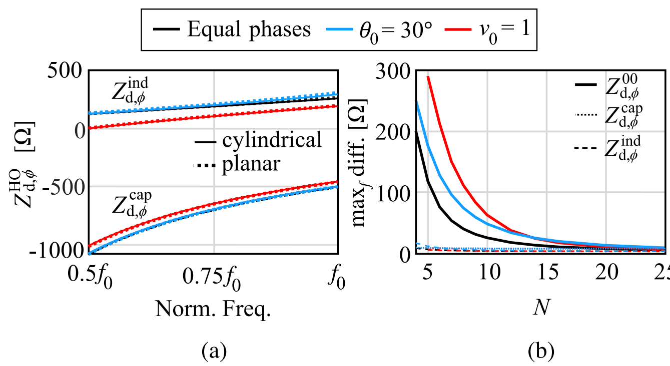

Fig. 17. (a) Higher order active input impedance of connected ϕ-oriented dipole for different scanning conditions ($N = 5$) and (b) maximum difference between cylindrical and planar array impedance as a function of N. The geometrical parameters are as defined in Fig. 4.

A similar split can be also made for the dipoles along z, with the difference that the m_y-modes are related to the inductance and the m_z-modes are related to the capacitance. The three terms can be represented as the equivalent circuit in Fig. 14(a). The equivalent circuit representation for the slots is also shown in Fig. 14(b).

For the ϕ-connected dipoles, when studying the variations of the separate fundamental and higher order components of the impedance versus N, the curves in Fig. 15 are obtained. It is evident that the fundamental mode varies significantly with N, as it is associated with a radiated cylindrical wave with changing curvature. Only for large N, the fundamental mode approaches the solution for the planar case. On the contrary, the higher order components of the impedance appear to be independent on N. This can be interpreted with the fact that the reactive energy, associated with the capacitance of the feed and the inductance of the dipole, is a localized effect mainly related to feed length δ_d and the dipole width w_d, and thus weakly dependent on the curvature.

This finding can be exploited to overcome the numerical issues described in Section IV-A, by approximating the higher order impedance of the cylindrical array with the one of the planar geometry, which is numerically stable

$$Z_{\mathrm{d},\phi} \approx Z^{\mathrm{cap}}_{\mathrm{d,planar}} \,\|\, \left(Z^{\mathrm{ind}}_{\mathrm{d,planar}} + Z^{00}_{\mathrm{d},\phi}\right) \tag{34}$$

where the expressions of $Z^{\mathrm{cap}}_{\mathrm{d,planar}}$ and $Z^{\mathrm{ind}}_{\mathrm{d,planar}}$ were reported in [46].

The planar equivalent array is defined as the array that scans to the same direction of the cylindrical array with respect to the normal to the feed at its center. Please note that, for $\nu_0 \neq 0$, which corresponds to a phase shift along the circumference of $\Delta\phi = 2\pi\nu_0/N$, the equivalent planar array would scan to an angle that changes with frequency $\theta_0(f) = \mathrm{asin}[\Delta\phi/(k_0 l_{\mathrm{arc}})]$, as depicted in Fig. 16.

The approximation of the higher order terms by the planar problem remains valid in all the scanning conditions, as shown in Fig. 17. The impedance associated with the higher order modes is always equal to the equivalent planar array, as shown in Fig. 17(a), for equal phase, for scanning to $\theta_0 = 30°$, and for $\nu_0 = 1$. Moreover, one can plot the maximum absolute difference, over the frequency band, between the cylindrical and the planar array solution ($\max_f |Z_{\mathrm{d},\phi}(N) - Z_{\mathrm{d,planar}}|$) as a function of N for the fundamental mode and the higher order modes, as shown in Fig. 17(b). For all considered scanning cases, unlike the fundamental mode, the higher order modes converge to the planar array for very small N. We also note that, for unequal phase excitation, the convergence of fundamental mode to the planar arrays is slower with N.

Although this study has been presented for ϕ-connected dipoles, we observe similar behavior for z-connected dipoles and both slot polarizations. The separation of the impedance terms for the slots, represented by the circuit in Fig. 14(b), allows the convergence study for increasing radius of curvature for the connected slots. This is reported in Fig. 18, for z- and ϕ-oriented slots. Also for this geometry, the array curved in the E-plane requires a larger N to converge to the planar array solution.

V. Conclusion

We presented a unit-cell analysis for cylindrically connected arrays. The main contributions and insights of this work can be summarized as follows.

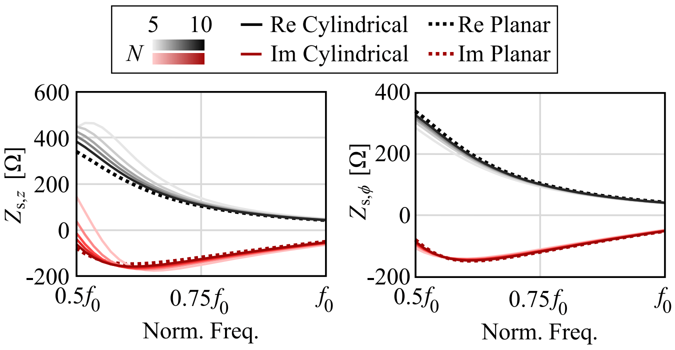

(a) (b)

Fig. 18. Active input impedance of connected slot unit cell versus N. (a) Slots along z and (b) slots along ϕ. The geometrical parameters are as defined in Fig. 4, for varying N and with $w_s = \delta_s = \lambda_0/20$.

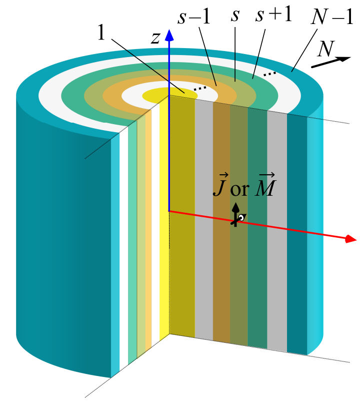

Fig. 19. Elementary electric $\vec{J}$ or magnetic $\vec{M}$ source radiating in cylindrically stratified media.

1) Analytical expressions for the active impedance were derived for both connected slots and dipoles in the presence of a cylindrical reflector. These expressions enable efficient computation of the active impedance with significantly reduced computational cost, making them well suited for the optimization of the array's geometrical parameters.
2) Model was extensively validated through comparisons with the commercial software Ansys HFSS. Arrays in both free space and cylindrically stratified media were considered, demonstrating the accuracy of the proposed method in each case.
3) Challenges associated with the numerical implementation of higher order cylindrical Floquet modes were addressed, and an efficient approximation was proposed in which the higher order impedance modes of the cylindrical geometry are modeled using the equivalent planar geometry.
4) This enables the study of the variation of input impedance with the radius of curvature. Due to mutual coupling, the array curved in its E-plane is more affected by the curvature and converges slower to the planar case for increasing radius of curvature, compared to the array curved in its H-plane.

Appendix
Derivation of Relevant Spectral Green's Functions

In this appendix, we summarize the derivation of the spectral Green's function in cylindrically stratified media. Fig. 19 shows a general dielectric stratification with N layers, invariant with respect to z and ϕ. The different dielectric layers have index i, with the outer infinite layer having index $i = N$. We assume an elementary electric ($\vec{J}$) or magnetic ($\vec{M}$) source to be located in the sth layer, at $\vec{r}' = (\rho', \phi', z')$. The source is polarized in the α-direction, where $\hat{\alpha}$ can be either $\hat{z}$ or $\hat{\phi}$.

Following [32], in cylindrical coordinates, the $z\alpha$-component of the spatial dyadic Green's function ($g_{z\alpha}$) can be expressed as the inverse Fourier transform of its spectral counterpart ($G_{z\alpha}$)

$$g_{z\alpha}^{FC}\left(\vec{r}, \vec{r}'\right) = \sum_m e^{-jm(\phi-\phi')} \times \frac{1}{2\pi}\int_{-\infty}^{\infty} G_{z\alpha}^{FC}\left(m, k_z, \rho, \rho'\right) e^{-jk_z(z-z')} dk_z \quad (35)$$

where $\vec{r} = (\rho, \phi, z)$ is the observation point, the superscript F can represent either the electric (E) or the magnetic (H) field, and the superscript C can refer to either the electric (J) or the magnetic (M) source. A general expression of the $z\alpha$-components of the electric and magnetic Green's function that is valid in cylindrically stratified media, in the dielectric layer where the source is located, is given in [32] as

$$\begin{bmatrix} G_{z\alpha}^{EC}\left(m, k_z, \rho, \rho'\right) \\ G_{z\alpha}^{HC}\left(m, k_z, \rho, \rho'\right) \end{bmatrix} = \frac{-1}{4\omega}\left\{J_m\left(k_\rho \rho_<\right) H_m^{(2)}\left(k_\rho \rho_>\right)\bar{\mathbf{I}} + \bar{\mathbf{a}}_{m,s}\left(\rho'\right) H_m^{(2)}\left(k_\rho \rho\right) + \bar{\mathbf{b}}_{m,s}\left(\rho'\right) J_m\left(k_\rho \rho\right)\right\} \cdot \overleftarrow{\mathbf{D}}'_C \quad (36)$$

where ω is the angular frequency, $k_\rho = (k^2 - k_z^2)^{1/2}$, k is the wavenumber in the source layer, $\rho_< = \min(\rho, \rho')$, $\rho_> = \max(\rho, \rho')$, $\bar{\mathbf{I}}$ is the 2 by 2 identity matrix, $\bar{\mathbf{a}}_{m,s}$ and $\bar{\mathbf{b}}_{m,s}$ are 2 by 2 matrices that depend on the boundary conditions in the cylindrical stratification. The three terms between braces in (36) represent the impressed field due to the source, the outgoing wave component due to reflections, and the standing wave component due to reflections in the source layer s, respectively. The vector operator $\overleftarrow{\mathbf{D}}'_C$ depends on the source being electric

$$\overleftarrow{\mathbf{D}}'_J = \begin{bmatrix} \frac{1}{\varepsilon}\left(k^2\hat{z} + jk_z\nabla'\right)\cdot\hat{\alpha} \\ j\omega\hat{z}\cdot\nabla'\times\hat{\alpha} \end{bmatrix} \quad (37)$$

or magnetic

$$\overleftarrow{\mathbf{D}}'_M = \begin{bmatrix} -j\omega\hat{z}\cdot\nabla'\times\hat{\alpha} \\ \frac{1}{\mu}\left(k^2\hat{z} + jk_z\nabla'\right)\cdot\hat{\alpha} \end{bmatrix} \quad (38)$$

and acts on the functions to its left, as indicated by the arrow. The dielectric layer containing the source is characterized by permittivity ε and permeability μ. The nabla operator is given as follows in the spectral domain:

$$\nabla' = \hat{\rho}\frac{\partial}{\partial\rho'} + \hat{\phi}\frac{jm}{\rho'} + \hat{z}jk_z. \quad (39)$$

For some of the analyzed connected array geometries, the $\phi\phi$-component of the dyadic spectral Green's function is needed. In cylindrical coordinates, for a homogeneous medium, the z-transverse electric ($\vec{E}_t$) and magnetic ($\vec{H}_t$) fields can be derived from the z-components as [32]

$$\vec{E}_t = \frac{1}{k_\rho^2}(-jk_z\nabla_t E_z - j\omega\mu\nabla_t \times \hat{z}H_z)$$
$$\vec{H}_t = \frac{1}{k_\rho^2}(-jk_z\nabla_t H_z + j\omega\varepsilon\nabla_t \times \hat{z}E_z) \quad (40)$$

with the transverse nabla operator expressed in cylindrical coordinates as follows:

$$\nabla_t = \hat{\rho}\frac{\partial}{\partial\rho} + \hat{\phi}\frac{1}{\rho}\frac{\partial}{\partial\phi}. \quad (41)$$

Applying the relations in (36)–(40) and recognizing from (35) that $\partial/\partial\phi \rightarrow -jm$ in the spectral domain, the $\phi\alpha$-components of the Green's functions can be derived from the $z\alpha$-components as

$$\begin{bmatrix} G_{\phi\alpha}^{EC}(m,k_z,\rho,\rho') \\ G_{\phi\alpha}^{HC}(m,k_z,\rho,\rho') \end{bmatrix} = -\frac{1}{k_\rho^2}\begin{bmatrix} \frac{mk_z}{\rho} & -j\omega\mu\frac{\partial}{\partial\rho} \\ j\omega\varepsilon\frac{\partial}{\partial\rho} & \frac{mk_z}{\rho}\end{bmatrix} \cdot \begin{bmatrix} G_{z\alpha}^{EC}(m,k_z,\rho,\rho') \\ G_{z\alpha}^{HC}(m,k_z,\rho,\rho') \end{bmatrix}. \quad (42)$$

To derive the explicit expressions of the Green's function, the coefficients of the outgoing wave $\bar{\mathbf{a}}_{m,s}$ and the standing wave $\bar{\mathbf{b}}_{m,s}$ must be calculated. The coefficients are given as [32]

$$\bar{\mathbf{a}}_{m,s} = \left[\bar{\mathbf{I}} - \widetilde{\mathbf{R}}_{s,s-1}\cdot\widetilde{\mathbf{R}}_{s,s+1}\right]^{-1}\cdot\widetilde{\mathbf{R}}_{s,s-1} \cdot\left[H_m^{(2)}\left(k_{\rho,s}\rho'\right)\bar{\mathbf{I}} + J_m\left(k_{\rho,s}\rho'\right)\widetilde{\mathbf{R}}_{s,s+1}\right] \quad (43)$$
$$\bar{\mathbf{b}}_{m,s} = \left[\bar{\mathbf{I}} - \widetilde{\mathbf{R}}_{s,s+1}\cdot\widetilde{\mathbf{R}}_{s,s-1}\right]^{-1}\cdot\widetilde{\mathbf{R}}_{s,s+1} \cdot\left[J_m\left(k_{\rho,s}\rho'\right)\bar{\mathbf{I}} + H_m^{(2)}\left(k_{\rho,s}\rho'\right)\widetilde{\mathbf{R}}_{s,s-1}\right] \quad (44)$$

where the matrices $\widetilde{\mathbf{R}}_{s,s-1}$ and $\widetilde{\mathbf{R}}_{s,s+1}$, refer to the generalized backward and forward reflection matrices in the source layer s [32]. For any layer i, the generalized backward and forward reflection matrices can be calculated as follows:

$$\widetilde{\mathbf{R}}_{i,i-1} = \overline{\mathbf{R}}_{i,i-1} + \overline{\mathbf{T}}_{i-1,i}\cdot\widetilde{\mathbf{R}}_{i-1,i-2} \cdot\left(\bar{\mathbf{I}} - \overline{\mathbf{R}}_{i-1,i}\cdot\widetilde{\mathbf{R}}_{i-1,i-2}\right)^{-1}\cdot\overline{\mathbf{T}}_{i,i-1} \quad (45)$$
$$\widetilde{\mathbf{R}}_{i,i+1} = \overline{\mathbf{R}}_{i,i+1} + \overline{\mathbf{T}}_{i+1,i}\cdot\widetilde{\mathbf{R}}_{i+1,i+2} \cdot\left(\bar{\mathbf{I}} - \overline{\mathbf{R}}_{i+1,i}\cdot\widetilde{\mathbf{R}}_{i+1,i+2}\right)^{-1}\cdot\overline{\mathbf{T}}_{i,i+1} \quad (46)$$

where $\overline{\mathbf{R}}_{i,i-1}$ and $\overline{\mathbf{R}}_{i,i+1}$ are the local backward and forward reflection matrices, respectively. Similarly, $\overline{\mathbf{T}}_{i,i-1}$ and $\overline{\mathbf{T}}_{i,i+1}$ are the backward and forward transmission matrices, respectively. The generalized reflection matrices are calculated recursively by realizing that $\overline{\mathbf{R}}_{1,0} = 0$ and $\overline{\mathbf{R}}_{N,N+1} = 0$, where N is the index of the outer layer. The local reflection matrices are given by

$$\overline{\mathbf{R}}_{i,i+1} = \overline{\mathbf{D}}^{-1}\cdot\left[H_m^{(2)}\left(k_{\rho,i}a\right)\overline{\mathbf{H}}_m^{(2)}\left(k_{\rho,i+1}a\right) - H_m^{(2)}\left(k_{\rho,i+1}a\right)\overline{\mathbf{H}}_m^{(2)}\left(k_{\rho,i}a\right)\right] \quad (47)$$
$$\overline{\mathbf{R}}_{i,i-1} = \overline{\mathbf{D}}^{-1}\cdot\left[J_m\left(k_{\rho,i-1}a\right)\overline{\mathbf{J}}_m\left(k_{\rho,i}a\right) - J_m\left(k_{\rho,i}a\right)\overline{\mathbf{J}}_m\left(k_{\rho,i-1}a\right)\right] \quad (48)$$

with

$$\overline{\mathbf{D}} = \left[\overline{\mathbf{J}}_m(k_{\rho,i}a)H_m^{(2)}(k_{\rho,i+1}a) - \overline{\mathbf{H}}_m^{(2)}(k_{\rho,i+1}a)J_m(k_{\rho,i}a)\right]. \quad (49)$$

The matrices $\overline{\mathbf{J}}_m(k_{\rho,i}a)$ and $H_m^{(2)}(k_{\rho,i}a)$ are defined as

$$\overline{\mathbf{B}}_m\left(k_{\rho,i}\rho\right) = \frac{1}{k_{\rho,i}^2\rho} \times\begin{bmatrix} -j\omega\varepsilon_i k_{\rho,i}\rho B_m'\left(k_{\rho,i}\rho\right) & -mk_z B_m\left(k_{\rho,i}\rho\right) \\ -mk_z B_m\left(k_{\rho,i}\rho\right) & j\omega\mu_i k_{\rho,i}\rho B_m'\left(k_{\rho,i}\rho\right)\end{bmatrix} \quad (50)$$

where B_m can refer to either J_m or $H_m^{(2)}$, $k_{\rho,i}^2 = k_i^2 - k_z^2$, with k_i being the propagation constant of the ith medium. The forward and backward transmission matrices can be calculated in the following way:

$$\overline{\mathbf{T}}_{i,i+1} = \frac{2\omega}{\pi k_{\rho,i}^2 a}\overline{\mathbf{D}}^{-1}\cdot\begin{bmatrix}\varepsilon_i & 0 \\ 0 & -\mu_i\end{bmatrix} \quad (51)$$
$$\overline{\mathbf{T}}_{i,i-1} = \frac{2\omega}{\pi k_{\rho,i}^2 a}\overline{\mathbf{D}}^{-1}\begin{bmatrix}\varepsilon_i & 0 \\ 0 & -\mu_i\end{bmatrix}. \quad (52)$$

The general procedure described thus far can be used to derive the explicit expressions of the Green's functions for the specific problems in Fig. 20, needed to model the backing reflector and slot surface in connected arrays. The local reflection matrices can be calculated by imposing the PEC boundary condition, that is, vanishing tangential electric fields, at the respective boundaries, for the canonical external and internal problem, depicted in Fig. 20(a) and (b), respectively. For the analysis of connected dipole and slot arrays in free space, two canonical cases can be identified. The first case considers an elementary source, either electric or magnetic, located at $\rho = \rho'$ radiating at a distance h on top of a PEC cylinder of radius $\rho = a$, as illustrated in Fig. 20(a). Such a boundary results in the following coefficients for the outgoing and standing wave components, respectively.

$$\bar{\mathrm{a}}_{m,s} = H_m^{(2)}\left(k_\rho\rho'\right)\overline{\mathbf{R}}_{\text{ext}}, \quad \bar{\mathrm{b}}_{m,s} = 0 \quad (53)$$

with

$$\overline{\mathbf{R}}_{\text{ext}}(a) = \begin{bmatrix} -\frac{J_m(k_\rho a)}{H_m^{(2)}(k_\rho a)} & 0 \\ 0 & -\frac{J_m'(k_\rho a)}{H_m^{(2)'}(k_\rho a)}\end{bmatrix}. \quad (54)$$

Another canonical case one must consider is the one of a source located at $\rho = \rho'$ radiating inside a PEC cylinder of radius $\rho = \rho_0$, similar to the case of a circular waveguide, as show in Fig. 20(b). In such a geometry, the amplitude of the outgoing and standing wave components can be found as follows:

$$\bar{\mathrm{a}}_{m,s} = 0, \quad \bar{\mathrm{b}}_{m,s} = J_m\left(k_\rho\rho'\right)\overline{\mathbf{R}}_{\text{int}} \quad (55)$$

with

$$\overline{\mathbf{R}}_{\text{int}}(\rho_0) = \begin{bmatrix} -\frac{H_m^{(2)}(k_\rho\rho_0)}{J_m(k_\rho\rho_0)} & 0 \\ 0 & -\frac{H_m^{(2)'}(k_\rho\rho_0)}{J_m'(k_\rho\rho_0)}\end{bmatrix}. \quad (56)$$

The reflection matrices and hence the coefficients $\bar{\mathbf{a}}_{m,s}$ and $\bar{\mathbf{b}}_{m,s}$ only depend on the geometry of the stratification and the source location, since the source type (electric or magnetic) is taken into account through the operator $\overleftarrow{\mathbf{D}}_C'$ in (36).

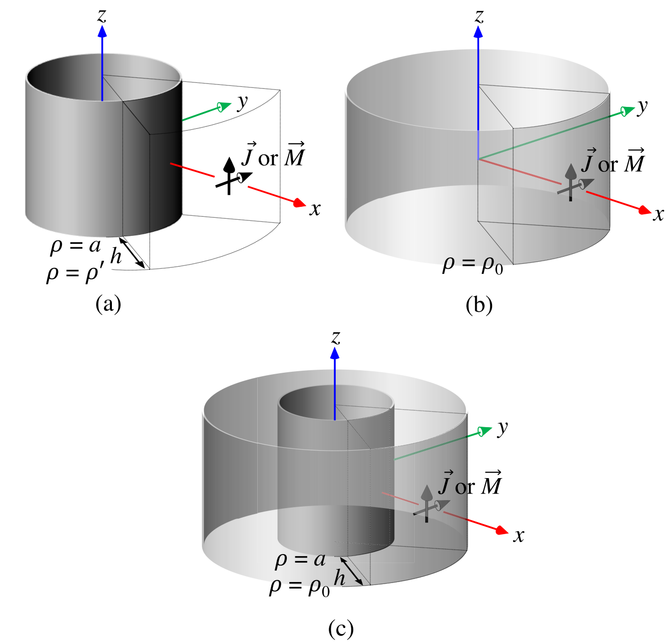

Fig. 20. Elementary source (a) located outside a PEC cylinder infinite along z, (b) inside a PEC cylinder (cylindrical cavity), and (c) in between two PEC cylinders (coaxial cavity).

The aforementioned reflection matrices can be used to derive the Green's function of the more complex structure depicted in Fig. 20(c), which represents a coaxial cavity bounded by two cylinders of radii a and ρ_0 and a source located at $\rho' \in [a, \rho_0]$. In this case, the amplitude of the outgoing and standing wave are given as follows:

$$\begin{aligned}\bar{\mathrm{a}}_{m,s} &= \left[\bar{\mathbf{I}} - \bar{\mathbf{R}}_{\mathrm{ext}} \cdot \bar{\mathbf{R}}_{\mathrm{int}}\right]^{-1} \\ &\quad \cdot \bar{\mathbf{R}}_{\mathrm{ext}} \cdot \left[H_m^{(2)}\left(k_\rho \rho'\right) \bar{\mathbf{I}} + J_m\left(k_\rho \rho'\right) \bar{\mathbf{R}}_{\mathrm{int}}\right] \\ \bar{\mathrm{b}}_{m,s} &= \left[\bar{\mathbf{I}} - \bar{\mathbf{R}}_{\mathrm{int}} \cdot \bar{\mathbf{R}}_{\mathrm{ext}}\right]^{-1} \\ &\quad \cdot \bar{\mathbf{R}}_{\mathrm{int}} \cdot \left[J_m\left(k_\rho \rho'\right) \bar{\mathbf{I}} + H_m^{(2)}\left(k_\rho \rho'\right) \bar{\mathbf{R}}_{\mathrm{ext}}\right] \end{aligned} \tag{57}$$

where the reflection matrices are given in (54) and (56).

References

[1] L. Josefsson and P. Persson, *Conformal Array Antenna Theory Design*, 1st ed., Hoboken, NJ, USA: Wiley, 2006.

[2] R. J. Mailloux, *Phased Array Antenna Handbook*, 3rd ed., Norwood, MA, USA: Artech House, 2017.

[3] J.-J. Peng, S.-W. Qu, M. Xia, and S. Yang, "Conformal phased array antenna for unmanned aerial vehicle with ±70° scanning range," *IEEE Trans. Antennas Propag.*, vol. 69, no. 8, pp. 4580–4587, Aug. 2021.

[4] D. Nikolayev, Ì. V. Soares, A. Mazzinghi, and A. K. Skrivervik, "Conformal beam-scanning arrays: Survey, analysis, and benchmarking," *IEEE Antennas Propag. Mag.*, vol. 67, no. 4, pp. 6–17, Aug. 2025.

[5] J. T. Logan, W. M. Dorsey, and J. A. Valenzi, "Modular all-metal ultra-wideband cylindrical array for multifunction operation," *IEEE Trans. Antennas Propag.*, vol. 70, no. 10, pp. 9175–9183, Oct. 2022.

[6] L. Shestag, "A cylindrical array for the TACAN system," *IEEE Trans. Antennas Propag.*, vol. AP-22, no. 1, pp. 17–25, Jan. 1974.

[7] C. Fulton et al., "Cylindrical polarimetric phased array radar: Beamforming and calibration for weather applications," *IEEE Trans. Geosci. Remote Sens.*, vol. 55, no. 5, pp. 2827–2841, May 2017.

[8] R. W. Kindt and W. R. Pickles, "Ultrawideband all-metal flared-notch array radiator," *IEEE Trans. Antennas Propag.*, vol. 58, no. 11, pp. 3568–3575, Nov. 2010.

[9] D. H. Schaubert, S. Kasturi, A. O. Boryssenko, and W. M. Elsallal, "Vivaldi antenna arrays for wide bandwidth and electronic scanning," in *Proc. 2nd Eur. Conf. Antennas Propag.*, Nov. 2007, pp. 1–6.

[10] J. T. Logan, R. W. Kindt, M. Y. Lee, and M. N. Vouvakis, "A new class of planar ultrawideband modular antenna arrays with improved bandwidth," *IEEE Trans. Antennas Propag.*, vol. 66, no. 2, pp. 692–701, Feb. 2018.

[11] Y. Zhou et al., "Tightly coupled array antennas for ultra-wideband wireless systems," *IEEE Access*, vol. 6, pp. 61851–61866, 2018.

[12] J. J. Lee, S. Livingston, R. Koenig, D. Nagata, and L. L. Lai, "Compact light weight UHF arrays using long slot apertures," *IEEE Trans. Antennas Propag.*, vol. 54, no. 7, pp. 2009–2015, Jul. 2006.

[13] R. Ozzola, A. Neto, U. Imberg, and D. Cavallo, "Connected slot array with interchangeable ADL radome for sub-8 GHz 5G applications," *IEEE Trans. Antennas Propag.*, vol. 72, no. 1, pp. 992–997, Jan. 2024.

[14] A. Boryssenko and T. Goodwin, "Broadband antenna array aperture made of tightly couple printed dipoles," in *Proc. IEEE Int. Symp. Phased Array Syst. Technol. (PAST)*, Oct. 2016, pp. 1–6.

[15] S. Xiao, S. Yang, H. Zhang, Q. Xiao, Y. Chen, and S.-W. Qu, "Practical implementation of wideband and wide-scanning cylindrically conformal phased array," *IEEE Trans. Antennas Propag.*, vol. 67, no. 8, pp. 5729–5733, Aug. 2019.

[16] S. Hussain, S.-W. Qu, P. Zhang, X.-H. Wang, and S. Yang, "A low-profile, wide-scan, cylindrically conformal X-band phased array," *IEEE Antennas Wireless Propag. Lett.*, vol. 20, pp. 1503–1507, 2021.

[17] H. S. Youn, Y. L. Lee, N. Celik, and M. F. Iskander, "Design of a cylindrical long-slot array antenna integrated with hybrid EBG/ferrite ground plane," *IEEE Antennas Wireless Propag. Lett.*, vol. 11, pp. 180–183, 2012.

[18] J. Rayno, N. Celik, and M. F. Iskander, "Dual-polarization cylindrical long-slot array (CLSA) antenna integrated with compact broadband baluns and slot impedance transformers," *IEEE Antennas Wireless Propag. Lett.*, vol. 12, pp. 1384–1387, 2013.

[19] J.-C. Sureau and A. Hessel, "Element pattern for circular arrays of waveguide-fed axial slits on large conducting cylinders," *IEEE Trans. Antennas Propag.*, vol. AP-19, no. 1, pp. 64–74, Jan. 1971.

[20] G. Borgiotti and Q. Balzano, "Mutual coupling analysis of a conformal array of elements on a cylindrical surface," *IEEE Trans. Antennas Propag.*, vol. AP-18, no. 1, pp. 55–63, Jan. 1970.

[21] A. Munger, J. Provencher, and B. Gladman, "Mutual coupling on a cylindrical array of waveguide elements," *IEEE Trans. Antennas Propag.*, vol. AP-19, no. 1, pp. 131–134, Jan. 1971.

[22] G. Gerini and L. Zappelli, "Phased arrays of rectangular apertures on conformal cylindrical surfaces: A multimode equivalent network approach," *IEEE Trans. Antennas Propag.*, vol. 52, no. 7, pp. 1843–1850, Jul. 2004.

[23] S. Raffaelli, Z. Sipus, and P.-S. Kildal, "Analysis and measurements of conformal patch array antennas on multilayer circular cylinder," *IEEE Trans. Antennas Propag.*, vol. 53, no. 3, pp. 1105–1113, Mar. 2005.

[24] J.-M. Jin, J. A. Berrie, R. Kipp, and S.-W. Lee, "Calculation of radiation patterns of microstrip antennas on cylindrical bodies of arbitrary cross section," *IEEE Trans. Antennas Propag.*, vol. 45, no. 1, pp. 126–132, Jan. 1997.

[25] F. Keshmiri and C. Craeye, "Moment-method analysis of normal-to-body antennas using a Green's function approach," *IEEE Trans. Antennas Propag.*, vol. 60, no. 9, pp. 4259–4270, Sep. 2012.

[26] C. Tokgoz and G. Dural, "Closed-form Green's functions for cylindrically stratified media," *IEEE Trans. Microw. Theory Techn.*, vol. 48, no. 1, pp. 40–49, Jan. 2000.

[27] S. Karan and V. B. Erturk, "Closed-form green's functions in cylindrically stratified media for method of moments applications," in *Proc. Int. Conf. Electromagn. Adv. Appl.*, Turin, Italy, Sep. 2009, pp. 473–476.

[28] T. Bertuch, F. Vipiana, and G. Vecchi, "Efficient analysis of printed structures of arbitrary shape on coated cylinders via spatial-domain mixed-potential Green's function," *IEEE Trans. Antennas Propag.*, vol. 60, no. 3, pp. 1425–1439, Mar. 2012.

[29] D. Bhattacharya, B. Ghosh, and K. Sarabandi, "Evaluation of efficient closed-form Green's function in a cylindrically stratified medium," *IEEE Trans. Antennas Propag.*, vol. 65, no. 3, pp. 1505–1510, Mar. 2017.

[30] J. Herper, A. Hessel, and B. Tomasic, "Element pattern of an axial dipole in a cylindrical phased array, Part I: Theory," *IEEE Trans. Antennas Propag.*, vol. AP-33, no. 3, pp. 259–272, Mar. 1985.

[31] Y. Gao, D. Wu, and Q. Wu, "Analysis of conformal antenna arrays using cylindrical periodic Green's function and RWG basis function," *IEEE Trans. Antennas Propag.*, vol. 72, no. 2, pp. 1385–1396, Feb. 2024.

[32] W. C. Chew, *Waves and Fields in Inhomogeneous Media*. Piscataway, NJ, USA: IEEE Press, 1995.
[33] K. Naishadham and L. B. Felsen, "Dispersion of waves guided along a cylindrical substrate-superstrate layered medium," *IEEE Trans. Antennas Propag.*, vol. 41, no. 3, pp. 304–313, Mar. 1993.
[34] Z. Sipus, P.-S. Kildal, R. Leijon, and M. Johansson, "An algorithm for calculating Green's functions for planar, circular cylindrical and spherical multilayer substrates," *Appl. Comput. Electromagn. Soc. J.*, vol. 13, no. 3, pp. 243–254, Nov. 1998.
[35] B. Biscontini, M. Burger, F. Demmel, and P. Russer, "Dyadic Green's function for conformal antennas in multi layered cylindrical structures using generalized transmission lines," in *Proc. Eur. Microw. Conf.*, Amsterdam, The Netherlands, 2004, pp. 953–956.
[36] C.-W. Lin and A. Grbic, "Analysis and synthesis of cascaded cylindrical metasurfaces using a wave matrix approach," *IEEE Trans. Antennas Propag.*, vol. 69, no. 10, pp. 6546–6559, Oct. 2021.
[37] B. Tomasic and N. Herscovici, "Analysis of cylindrical array of infinitely-long slots fed by connected dipoles," in *Proc. IEEE Antennas Propag. Soc. Int. Symp.*, North Charleston, SC, USA, Jun. 2009, pp. 1–4.
[38] A. Neto and J. J. Lee, "'Infinite Bandwidth' long slot array antenna," *IEEE Antennas Wireless Propag. Lett.*, vol. 4, pp. 75–78, 2005.
[39] A. Neto, D. Cavallo, G. Gerini, and G. Toso, "Scanning performances of wideband connected arrays in the presence of a backing reflector," *IEEE Trans. Antennas Propag.*, vol. 57, no. 10, pp. 3092–3102, Oct. 2009.
[40] D. Cavallo, "Connected slot antennas for wideband wide-scan phased arrays," in *Proc. IEEE Int. Symp. Phased Array Syst. Technol. (ARRAY)*, Boston, MA, USA, Oct. 2024, pp. 1–3.
[41] C. J. Fulton and A. Mirkamali, "A computer-aided technique for the analysis of embedded element patterns of cylindrical arrays [EM programmer's notebook]," *IEEE Antennas Propag. Mag.*, vol. 57, no. 3, pp. 132–138, Jun. 2015.
[42] R. Ozzola, D. Cavallo, and A. Neto, "On the relation between beam coupling and feed coupling in wideband antenna arrays," *IEEE Trans. Antennas Propag.*, vol. 70, no. 1, pp. 260–267, Jan. 2022.
[43] M. Abramowitz and I. A. Stegun, *Handbook of Mathematical Functions With Formulas, Graphs and Mathematical Tables*. New York, NY, USA: Dover, 1986.
[44] L. Felsen and N. Marcuvitz, *Radiation and Scattering of Waves*. Piscataway, NJ, USA: IEEE Press, 1994.
[45] D. E. Amos, "Algorithm 644: A portable package for Bessel functions of a complex argument and nonnegative order," *ACM Trans. Math. Softw.*, vol. 12, no. 3, pp. 265–273, Sep. 1986.
[46] D. Cavallo, A. Neto, and G. Gerini, "Green's function based equivalent circuits for connected arrays in transmission and in reception," *IEEE Trans. Antennas Propag.*, vol. 59, no. 5, pp. 1535–1545, May 2011.

Roderick G. Tapia Barroso (Graduate Student Member, IEEE) received the M.Sc. degree in electrical engineering from Delft University of Technology (TU Delft), Delft, The Netherlands, in 2023, where he is currently pursuing the Ph.D. degree in modeling and design of antenna arrays with the Terahertz Sensing Group.

His research interests include wideband wide-scan arrays, artificial dielectrics, modeling of cylindrical structures, and (semi-) analytical electromagnetic analysis methods.

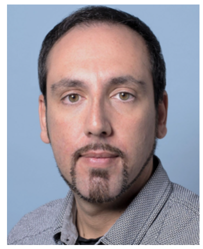

Daniele Cavallo (Senior Member, IEEE) received the M.Sc. degree (summa cum laude) in telecommunication engineering from the University of Sannio, Benevento, Italy, in 2007, and the Ph.D. degree (cum laude) in electromagnetics from Eindhoven University of Technology, Eindhoven, The Netherlands, in 2011.

From 2007 to 2011, he was with the Antenna Group, Netherlands Organization for Applied Scientific Research, The Hague, The Netherlands. From 2012 to 2015, he was a Post-Doctoral Researcher with the Microelectronics Department, Delft University of Technology (TU Delft), Delft, The Netherlands. In 2015, he joined the Chalmers University of Technology, Gothenburg, Sweden, as a Visiting Researcher. He is currently an Associate Professor with the Terahertz Sensing Group, TU Delft. He has authored or co-authored about 200 papers published in peer-reviewed international journals and conference proceedings. His current research interests include ultrawideband arrays, electromagnetic modeling of antennas, and millimeter-wave integrated arrays.

Dr. Cavallo received the Best Innovative Paper Prize from European Space Agency Antenna Workshop in 2008, the Best Paper Award in Electromagnetics and Antenna Theory from the 11th European Conference on Antennas and Propagation (EuCAP) in 2017, the Best Antenna Theory Paper from EuCAP 2024, and the "Veni" Personal Grant from the Netherlands Organization for Scientific Research in 2015. His students received several best paper awards at international conferences and multiple recognitions from Dutch foundations. He is the Co-Ordinator of European Association on Antennas and Propagation working group "Active Array Antennas." He served as the Technical Program Committee (TPC) Manager for the International Conference on Infrared, Millimeter, and Terahertz Waves in 2022 and the TPC Co-Chair for EuCAP 2024. He has served as an Associate Editor for IEEE TRANSACTIONS ON ANTENNAS AND PROPAGATION from 2016 to 2023.